JSST
Journal of Space Science and Technology

P-ISSN: 2008-4560
E-ISSN: 2423-4516

Journal of Space Science and Technology

Vol. 19, No. 3, pp. 56-70, 2026
https://doi.org/10.22034/jsst.2026.1583
Journal Homepage: https://jsstpub.com



Original Research Paper

Deep Recurrent Neural Networks for Predicting Supersonic Pressure Coefficient Distributions on Parametric Aerodynamic Geometries

Saleh Nemati* and Ramin Kamali Moghadam

Aerospace Research Institute, Ministry of Science, Research and Technology, Tehran, Iran

ARTICLE INFO

Article History:

Received 16 August 2025
Revised 29 November 2025
Accepted 18 February 2026
Available Online 01 september 2026

Keywords:

Neural networks
Supersonic flows
BiLSTM
Computational fluid Ddynamics (CFD)
Pressure coefficient

ABSTRACT

Accurate prediction of surface pressure distributions is critical for the aerodynamic analysis and design of high-speed axisymmetric bodies, particularly for configurations such as sphere-cone and flares. Traditional computational fluid dynamics (CFD) provides reliable results but is computationally expensive, especially when evaluating numerous geometrical variations. To address this challenge, we propose a Bidirectional Long Short-Term Memory (BiLSTM) network as a data-driven surrogate model for predicting the pressure coefficient (C_p) along axisymmetric surfaces. The BiLSTM leverages the sequential nature of surface geometry to learn both local and global flow features from a compact dataset of high-fidelity CFD simulations. Eighty geometries, each defined by seven key parameters, were simulated at Mach 2 using two-dimensional axisymmetric CFD under laminar flow assumptions. Comparative studies with feedforward neural networks (FNN) and unidirectional LSTM architectures demonstrate the superiority of the BiLSTM, achieving $R^2 = 0.985$ and a mean absolute error of 0.045. The results show that the bidirectional structure effectively captures forward and backward spatial correlations, yielding smooth and physically consistent C_p predictions, particularly near stagnation and flare compression zones. This framework provides a computationally efficient, high-fidelity, and generalizable approach for aerodynamic prediction, offering significant potential for rapid conceptual design and parametric studies of complex axisymmetric bodies.

*Corresponding Author's E-mail: canopusnier@gmail.com

How to Cite this Article:
S. Nemati and R. Kamali Moghadam, "Deep Recurrent Neural Networks for Predicting Supersonic Pressure Coefficient Distributions on Parametric Aerodynamic Geometries," *Journal of Space Science and Technology*, Vol. 19, No. 3, pp. 56-70, 2026, https://doi.org/10.22034/jsst.2026.1583.



COPYRIGHTS
© 2026 by the authors. Published by ARI. This article is an open access article distributed under the terms and conditions of The Creative Commons Attribution 4.0 International (CC BY 4.0).



NOMENCLATURE

CFD	Computational fluid dynamics
FNN	Feedforward neural networks
RNN	Recurrent neural networks
R^2	Coefficient of determination
BiLSTM	Bidirectional long short-term memory
C_p	Pressure coefficient

1. INTRODUCTION

Accurate prediction of aerodynamic parameters is essential for the analysis and design of aerodynamic bodies. One of the most fundamental of these parameters is the pressure coefficient (C_p), which quantifies the surface pressure distribution in response to external flow conditions. It plays a key role in determining both local pressure loads and overall aerodynamic behavior and is often used as a basis for computing other critical coefficients such as drag, lift, and moment. Consequently, precise knowledge of C_p is vital for evaluating stability, control, and thermal protection performance.

Aerodynamic designs, such as sphere-cone /flare configurations, are commonly favored due to their aerodynamic stability and favorable heat-shielding characteristics. However, evaluating their performance across a wide range of geometrical variations is computationally intensive. Generally, aerodynamic behavior is governed by systems of ordinary or partial differential equations (ODEs or PDEs), which define the relationship between input variables (e.g., geometry, flow conditions) and output responses (e.g., C_p , forces, heat flux). Computational Fluid Dynamics (CFD) [1] approximates these governing equations to simulate flow behavior under specific conditions. Despite its reliability, CFD has several limitations: (a) its accuracy is sensitive to mesh quality; (b) it is computationally expensive, especially in 3D high-speed flows; and (c) certain complex flows may not yield numerical solutions due to the nature of the governing equations [2]. Researchers have increasingly turned to machine learning approaches, particularly deep neural networks. Many studies have highlighted the growing capabilities and advantages of machine-learning methods [3, 4]. These techniques have been successfully applied across a wide range of fields, including combustion [5], materials property prediction [6] and aeronautics [7, 8], where they have demonstrated significant improvements in modeling efficiency and accuracy. Aerodynamic data modeling refers to the approximation of the mapping function between input and output data using appropriate models [9], and neural networks—being data-driven—have shown strong potential in this area. Unlike traditional CFD, neural networks do not require explicit knowledge of the physical governing equations. Instead, they learn complex mappings directly from data, enabling efficient and scalable prediction pipelines. They have achieved remarkable success across domains such as computer vision and are now being explored for their ability to model high-dimensional, multiscale, and nonlinear systems. The advantages of applying neural networks to aerodynamic data modeling are particularly evident when dealing with the complexities of fluid flow. Flow fields often exhibit both spatial and temporal variations, and their distribution is highly nonuniform. As a result, aerodynamic modeling presents several challenges for neural networks: (a) capturing the underlying physical mechanisms of unsteady or nonlinear flows; (b) addressing phenomena such as turbulence that are difficult to resolve using conventional CFD; and (c) extracting meaningful representations from limited datasets [10]. These challenges call for neural architectures capable of expressing long-range dependencies and learning rich feature representations from limited structured data.

Recent advances in aerodynamic prediction have increasingly leveraged machine-learning and deep-learning methodologies as efficient surrogates to CFD, particularly in the domain of pressure-coefficient and flow-field estimation. For instance, surrogate regression models have been applied successfully to aerodynamic-coefficient prediction using support-vector machines and neural networks [11]. Teimourian et al. [12] evaluated multiple algorithms, including Random Forest and Gradient Boosting, for predicting airfoil lift-to-drag ratios, highlighting the trade-offs between accuracy and computational speed in surrogate applications. Similarly, Zhang and Zhao [13] proposed a dimensionality reduction-based approach using neural networks to model flow fields around distributed structures like wind turbines, achieving scalable predictions with reduced data requirements. Negoita and Hothazaie [14] developed a deep neural

network model trained on CFD-generated data to forecast aerodynamic coefficients, emphasizing its utility for rapid airfoil assessments. More recently, deep-learning frameworks have extended toward full flow-field reconstruction (e.g., velocity/pressure distributions) on airfoils and wings by treating the geometry and flow field as images or tensors[15, 16]. Catalani et al. [17] advanced scalable neural field models for large-scale aerodynamics, demonstrating order-of-magnitude accuracy improvements for 2D airfoils and 3D aircraft. Sterpu et al. [16] investigated neural network ensembles for airfoil performance prediction, revealing the impact of random seed initialization on error variability and proposing ensembles for enhanced reliability in lift and drag estimates. Beyond 2D airfoils, studies have begun applying point-cloud and graph-neural-network methods to three-dimensional vehicle configurations, enabling prediction of distributed surface pressure on complex shapes [18]. Convolutional neural network (CNN) approaches have demonstrated strong performance in mapping high-dimensional geometry and flow-field data to pressures and loads in subsonic and transonic regimes [19]. These studies collectively underscore the shift toward data-efficient, transferable surrogates that address high-fidelity CFD challenges in pressure prediction, paving the way for sequence-based models like BiLSTM to fill gaps in axisymmetric and multi-Mach applications.

Recent works have explored the use of deep learning—especially recurrent architectures—for such modeling tasks. Li et al. [20] employed LSTM networks to predict aerodynamic and aeroelastic responses of a transonic NACA64A010 airfoil using flow parameters such as Mach number, pitch angle, and plunging displacement as inputs, and lift and moment coefficients as outputs. Other studies have combined Long Short-Term Memory (LSTM) networks with Proper Orthogonal Decomposition (POD) to construct reduced-order models that capture the temporal dynamics of turbulent flows [21], and to reconstruct time-resolved flow fields from sparse, discrete measurements [22]. Modular deep learning frameworks have also been introduced to build non-intrusive reduced-order models based solely on state snapshots, without requiring knowledge of the governing equations [23]. Wang et al [24] used geometric points in order to represent shape effects on the flow field. These works highlight the versatility and power of deep learning for aerodynamic and fluid dynamic modeling, particularly in complex, data-limited regimes.

Despite this progress, existing machine-learning-assisted aerodynamic models remain limited in scope. For example, k-Nearest Neighbors (k-NN) methods [25] have been applied to spike–blunt bodies to predict global drag characteristics over varying Mach numbers [26], but such approaches focus solely on integral aerodynamic quantities and do not address the more demanding problem of predicting full surface pressure distributions. Moreover, many studies employ simplified geometric descriptors or low-dimensional parameterizations, restricting their ability to generalize to arbitrary blunt-nose shapes. In contrast, predicting the complete C_p distribution along continuously varying axisymmetric surfaces requires the model to resolve both global aerodynamic trends and localized flow phenomena, including stagnation regions, compression zones, and expansion waves—features that cannot be captured by point-based or low-dimensional models.

In addition, deep learning has been extended to full three-dimensional aerodynamic prediction. A notable example is a PointNet [27] based framework trained on approximately 2000 shuttle-like geometries to predict entire pressure distributions under hypersonic conditions [28]. Although the model demonstrates impressive accuracy, its methodology differs fundamentally from the present study: it treats geometry as an unordered point cloud rather than an ordered sequence, does not exploit the intrinsic one-dimensional spatial continuity of axisymmetric surfaces, and requires expensive 3D Euler simulations at a single Mach number. These limitations underscore the need for lightweight, sequence-aware models capable of learning detailed pressure distributions from modest datasets.

The present study addresses these gaps by developing a Bidirectional Long Short-Term Memory (BiLSTM) model that treats axisymmetric surface geometries as ordered sequences, enabling high-resolution C_p predictions using compact descriptors and limited CFD data. This sequence-aware approach captures local phenomena like stagnation peaks, compressions, and expansions, offering a lightweight, data-efficient alternative to complex 3D methods.

In this study, a BiLSTM-based architecture is developed to predict C_p distributions from geometric inputs. Although primarily associated with temporal sequence modeling, BiLSTMs are

well suited to geometric sequences in which the pressure at any location depends on both upstream and downstream surface features. The dataset consists of 80 axisymmetric geometries defined by seven key parameters (including nose diameter, spherical-cap radius, cone angles, and body length), simulated at Mach 2 under laminar flow conditions using two-dimensional axisymmetric CFD in COMSOL Multiphysics. The proposed model achieves a coefficient of determination of R^2=0.985 with a mean absolute error of 0.045, demonstrating its potential as a highly efficient and accurate surrogate for high-fidelity CFD.

The remainder of this paper is organized as follows. Section 2 describes the CFD methodology and dataset generation. Section 3 outlines the BiLSTM architecture and training procedures. Section 4 presents prediction results and comparative analyses. Section 5 summarizes key conclusions and discusses directions for future work.

2. CFD METHODOLOGY AND DATASET GENERATION

To generate the training data for the neural network, a series of axisymmetric CFD simulations were conducted for a range of geometries. The flow was assumed to be steady and laminar, appropriate for the selected flow conditions, and all simulations were performed using the COMSOL 6.3 Multiphysics software.

2.1 Geometry Parameterization

The geometric configuration of the bodies used in this study is based on a sphere-cone with a rear flare, a well-established design different application. The geometry is fully described using six independent shape parameters, as illustrated in Fig. 1. These include the spherical nose radius R, the half-angle of the forebody cone α, the half-angle of the flare section β, the overall length of the body L,The maximum body diameter D, and the axial length of the cylindrical extension X. To account for spatial variation in pressure distribution along the body surface, a seventh input variable is incorporated: the normalized surface distance from the stagnation point, expressed as s/D, where s is the distance measured along the surface from the stagnation point and D is the maximum diameter. This non-dimensional parameter enables the model to predict local pressure coefficients at arbitrary positions along the body, independent of the body scale.

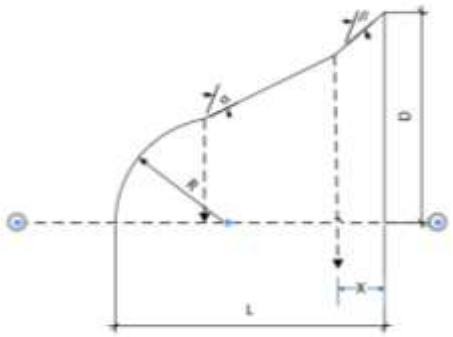


Fig. 1. Parametric definition of the sphere-cone geometry.

2.2 CFD Dataset Generation

The aerodynamic data used in this study was generated via high-fidelity numerical simulations of steady, compressible, laminar flow over aerodynamic geometries. We used the finite element method in a two-dimensional axisymmetric domain to solve the steady-state compressible Navier–Stokes equations, together with the continuity and energy equations.

In axisymmetric cylindrical coordinates (r, z), the steady continuity equation for compressible flow takes the form:

$$\frac{\partial(\rho u)}{\partial z}+\frac{1}{r}\frac{\partial(r\rho v)}{\partial r}=0 \quad (1)$$

where ρ is the density, u is the axial velocity, and v is the radial velocity component. The momentum equations in axial and radial directions are given by:

$$\rho u\frac{\partial v}{\partial z}+\rho v\frac{\partial v}{\partial r}=-\frac{\partial p}{\partial r}+\phi \quad (2)$$

$$\rho u\frac{\partial u}{\partial z}+\rho v\frac{\partial u}{\partial r}=-\frac{\partial p}{\partial z}+\phi \quad (3)$$

where p denotes static pressure. ϕ is Viscous terms which account for molecular viscosity μ. μ is calculated using Sutherland's law, a temperature-dependent model expressed as:

$$\mu(T)=\mu_0\left(\frac{T}{T_0}\right)^{3/2}\frac{T_0+c}{T+c} \quad (4)$$

with constants μ_0, T_0, and c, empirically determined for air. The energy equation, also steady-state and axisymmetric, includes conduction and viscous

dissipation terms and is closed using the ideal gas law:

$$p = \rho RT \quad (5)$$

where R is the specific gas constant for air. A constant value of γ=1.4 was assumed for the ratio of specific heats.

The computational domain replicates an axisymmetric shape placed in a supersonic freestream. Freestream boundary conditions were set as: pressure p_∞=2891 Pa, temperature T_∞=219 K, and velocity v_∞=596 m/s, corresponding to a freestream Mach number of approximately 2.0. The inflow boundary enforces all flow variables based on these freestream values. Along the body wall, no-slip conditions were applied for velocity, and an adiabatic thermal condition was imposed to neglect heat transfer. At the outflow boundary, a supersonic outlet condition allows for natural extrapolation of variables. Along the symmetry axis, axisymmetric boundary conditions are enforced to reduce the three-dimensional problem to a 2D representation.

The pressure coefficient, c_p, was calculated at multiple surface locations and serves as the primary aerodynamic output. It is defined by:

$$c_p = \frac{2}{\gamma M_\infty}\left(\frac{p}{p_\infty} - 1\right) \quad (6)$$

where p is the local pressure on the body surface, p_∞ is the freestream pressure, γ is the ratio of specific heats, and M_∞ is the freestream Mach number. Pressure values were extracted along the body's surface and mapped against the s/D.

A total of 80 different geometries were simulated, varying in nose diameter, spherical cap radius, cone half-angles, overall length, and flare parameters. The resulting dataset forms the basis for the training and evaluation of the BiLSTM model described in Section 3. A representative mesh used in the simulations is shown in Fig. 2, illustrating the adaptive refinement applied near regions of high gradient, such as the stagnation zone and the flare junction.

Figure 3 illustrates the velocity magnitude distribution surrounding the blunt-body aerodynamic shape as obtained from the CFD simulation. The velocity approaches zero at the stagnation region, where the incoming flow encounters the front surface of the body, resulting in a strong deceleration due to normal shock compression. Downstream, the velocity increases rapidly as the flow is deflected and accelerates along the body contour. The high-speed region behind the body shows velocity magnitudes exceeding 600 m/s, indicating strong expansion and flow acceleration. This distribution clearly captures the aerodynamic effects of flow deceleration and reacceleration around blunt geometries, which are critical in pressure and thermal load assessments.

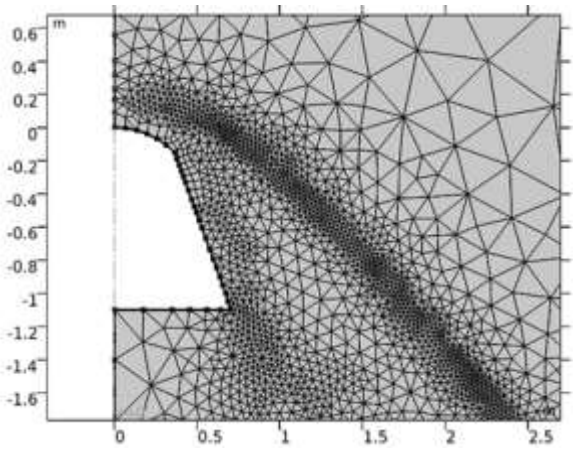


Fig. 2. Adaptive triangular mesh used for the 2D axisymmetric CFD simulation. The mesh is refined near the stagnation point and flare region to ensure accurate resolution of flow gradients in high Mach number conditions.

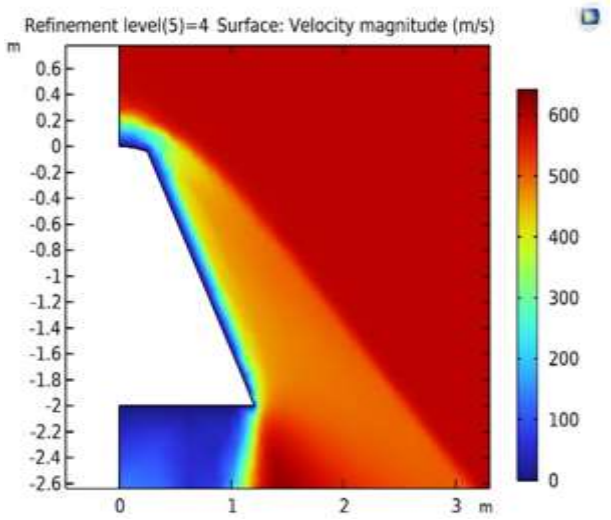


Fig. 3. Velocity magnitude contour around the shape, illustrating the deceleration at the stagnation point and acceleration of the flow along the body surface.

2.3 CFD Data Preprocessing

Each data point included a seven-dimensional input vector comprising the nose diameter, spherical

cap radius, two cone half-angles, overall length of the body, rear curvature and the normalized surface location, expressed as s / D.

the corresponding output value for each input vector was the local coefficient of pressure c_p, obtained through high-fidelity computational fluid dynamics simulations as described in Section 2.2. In the construction of the dataset, each surface point was treated as an independent sample. This approach allows the network to learn the underlying aerodynamic mapping without relying on sequential information or time-based dependencies.

The dataset was randomly divided into two parts: 70% of the data was used for training the network, 30% was allocated for validation during model development. Standardization of the input features and output was performed after the data split, based on the mean and standard deviation of the training set. This ensured consistent feature scaling while preventing data leakage from the test and validation subsets. Table 1 shows the parameters along their respected units used for model training.

Table 1. Geometric input features used for BiLSTM training.

Feature No.	Parameters	Unit
1	R	m
2	L	m
3	α	degrees
4	β	degrees
5	D	m
6	x	m
7	s/D	dimensionless

2.4 Mesh Independence Study

To verify the accuracy and stability of the CFD simulations, a mesh independence study was performed by progressively refining the computational grid through adaptive mesh iterations. The evaluation focused on two key aerodynamic quantities: the maximum surface pressure coefficient $C_{p\ max}$ and the mean surface pressure coefficient $C_{p\ mean}$. Mesh convergence was considered achieved when further refinement produced negligible changes (typically less than 1%) in these metrics.

The initial coarse grid (0 adaptations) contained 1,205 elements. Subsequent mesh adaptations were guided by COMSOL's built-in error estimators, which concentrate refinement in regions of high velocity and pressure gradients, such as the stagnation zone, shock layer, and the cone–flare junction. Table 2 presents the mesh refinement history for a representative geometry at Mach 2.0.

As seen in Table 2, $C_{p\ max}$ stabilizes at approximately 1.606 beyond adaptation level 3, with only a 0.06% difference between levels 4 and 5. The mean pressure coefficient shows similar behavior, converging to about 0.366–0.367 after level 3, with variations below 0.5% thereafter. These small differences confirm that the solution becomes effectively mesh-independent at adaptation level 4.

Accordingly, all CFD cases in the final dataset were computed using meshes refined to at least adaptation level 4 (typically 30,000–36,000 elements per geometry). This ensures that the resulting pressure distributions are sufficiently accurate for use in training the BiLSTM surrogate model while maintaining reasonable computational cost.

Table 2. Mesh independence study for a representative geometry (Mach 2.0).

Adaptation Level	Number of Elements	$C_{p\ max}$	$C_{p\ mean}$
0	1205	1.623	0.354
1	2749	1.576	0.378
2	6528	1.594	0.361
3	15338	1.605	0.365
4	34507	1.606	0.367
5	78262	1.606	0.366

2.5 CFD Model Validation

To ensure the accuracy and reliability of the CFD simulations used in this study, a validation step was performed by comparing the C_p distribution against results from a reference. The geometry for the simulation was designed to closely replicate the aerodynamic configuration in the work by Mehta [29] which includes both geometrical parameters and flow conditions.

Figure 4 shows the comparison between the C_p values computed in this work and those reported in the reference study. Both datasets are plotted as a function of the normalized surface distance (s/D).

The results demonstrate strong overall agreement in the trend and shape of the distribution. Minor discrepancies are observed, particularly near the rear of the body, which can be attributed to differences in mesh resolution, numerical schemes, or slight geometric deviations. This validation supports the use of the simulation setup for generating training data for the neural network model in subsequent sections.

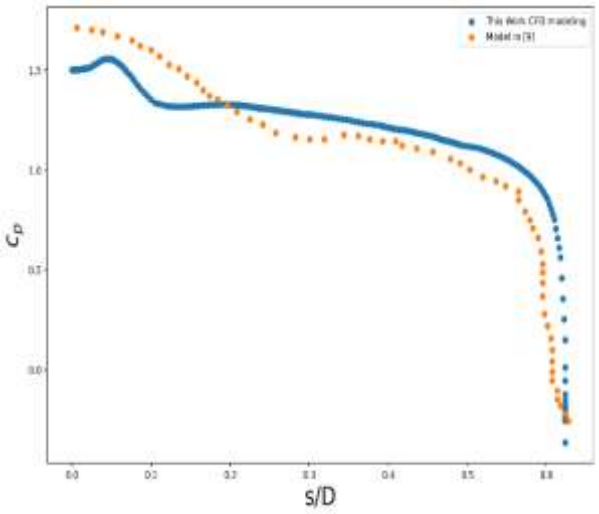


Fig. 4. Comparison of surface pressure coefficient (Cp) distribution along the normalized surface coordinate (s/D) between the present CFD modeling and the reference data from Mehta [19].

3. NEURAL NETWORK MODEL

To develop a robust surrogate model for predicting the pressure coefficient (c_p) from geometric parameters of aerodynamic body, a Bi-directional Long Short-Term Memory (BiLSTM) neural network was employed. This architecture effectively captures the underlying spatial dependencies across the normalized surface distance s/D by interpreting it as a one-dimensional sequence for each geometric configuration.

Recurrent Neural Networks (RNNs), unlike feedforward neural networks, incorporate a recurrent structure via feedback loops that allow hidden neurons to retain information from previous inputs. This temporal memory enables RNNs to model sequential data such as time-series or spatially distributed quantities [30, 31].

Despite their ability to model sequential data, traditional RNNs suffer from the vanishing gradient problem during training, which limits their ability to learn long-term dependencies [32, 33]. To overcome this, Long Short-Term Memory (LSTM) networks were proposed. Fig. 5 illustrates a typical LSTM cell. The cell consists of three different gates, namely, the forget gate f , input gate i and output gate o [34].

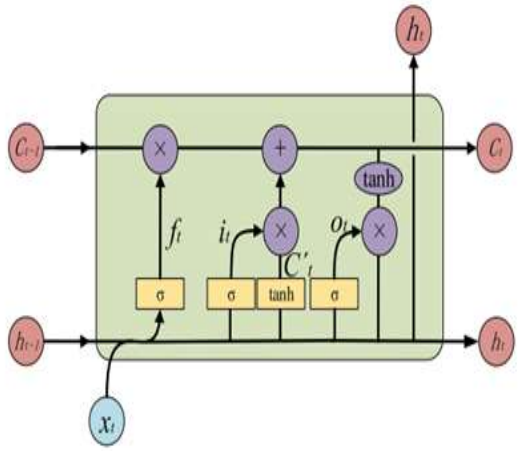


Fig. 5. The structure of the classic LSTM.

A forget gate determines what information should be discarded by an LSTM. The function of a forget gate can be formulated as in Equation 7, where h_{t-1} denotes the output of this cell at time t - 1, x_t denotes the input data of this cell at time t, and W_f and b_f denote the weights and biases of the forget gate, respectively. The activation function σ maps the input data to a specific range between 0 and 1. Consequently, some part of the input value will be discarded by the forget gate.

$$f_t = \sigma(W_f . [h_{t-1}, x_t] + b_f) \quad (7)$$

An input gate determines what information should be updated to the cell state. The function of an input gate can be formulated as in Equation 8 and 9, where $\acute{C}_t$ represents the provisional cell state calculated by the input gate, and it determines which parts of $\acute{C}_t$ should be added to the final state C_t. Equation 10 describes how the input gate updates the cell state C_t [34].

$$i_t = \sigma(W_i . [h_{t-1}, x_t] + b_i) \quad (8)$$

$$\acute{C}_t = tanh(W_c . [h_{t-1}, x_t] + b_c) \quad (9)$$

$$C_t = f_t \times C_{t-1} + i_t \times \acute{C}_t \quad (10)$$

The BiLSTM architecture was specifically selected because it can process input sequences in both forward and backward directions, allowing it to capture the interdependencies among geometric

parameters along the normalized surface distance (s/D). This bidirectional context improves the model's ability to represent spatial correlations and localized variations in C_p that arise from the geometric continuity of the blunt-body configuration. Compared with conventional LSTM or feedforward networks, BiLSTM provides enhanced feature extraction and smoother C_p predictions, especially in regions with strong gradient transitions such as the stagnation and flare zones.

The architecture consists of two BiLSTM layers with 128 and 64 units, respectively, followed by two dense layers with 64 and 32 neurons using ReLU activation. A final dense layer outputs the predicted C_p value. The model can be expressed as a nonlinear mapping:

$$\hat{C}_p = f_{NN}(X;\theta) \tag{11}$$

where $x \in R^7$ represents the geometric feature vector , θ denotes the network's trainable parameters and NN denotes neural networks. The network was trained using the Adam optimizer with a learning rate of 0.001 and the Mean Squared Error (MSE) as the loss function:

$$MSE = \frac{1}{N}\sum_{i=1}^{N}(C_{p,i} - \hat{C}_{p,i})^2 \tag{12}$$

In this study, each CFD sample corresponds to a single surface point and is represented by a seven-dimensional input vector containing the geometric descriptors listed in Table 1. The dataset for each geometry was sorted according to s/D so that the progression of points reflects the physical order along the body surface. When the data are provided to the BiLSTM in this sorted form, the model can naturally interpret the input as an ordered traversal from the stagnation region toward the aft section. In this way, the BiLSTM is able to learn smooth spatial trends in the pressure coefficient and capture upstream–downstream correlations driven by geometric continuity, even though each point is stored as an individual sample rather than as a predefined multi-step sequence.

All machine-learning models were implemented in Python using TensorFlow. The entire workflow—including preprocessing, normalization, training, and evaluation—was executed through fully scripted procedures to ensure reproducibility. Random seeds were fixed across all experiments, guaranteeing that identical model configurations yield consistent and unified results.

4. RESULTS AND DISCUSSION

In this section achieved results would be discussed.

4.1 Influence of Geometric Variation on Surface Pressure Distribution

To illustrate how geometric differences influence the aerodynamic response across the dataset, Fig. 6 presents four representative body configurations (left) together with their corresponding surface pressure coefficient (C_p) distributions as a function of normalized surface distance s/D (right). These examples highlight the diversity of shapes included in the dataset and demonstrate the range of surface-pressure behaviors that the BiLSTM model must learn to reproduce.

All four distributions show a characteristic stagnation-region pressure peak near s/D=0, consistent with the strong compression that forms ahead of forebodies in supersonic flow. The height and sharpness of this peak differ among the geometries due to variations in nose curvature: configurations with more abrupt leading-edge curvature produce a steeper rise in C_p, while smoother or more gradual curvature generates a broader, more diffuse peak.

Further downstream, the decaying portions of the C_p curves reflect how each geometry shapes the surrounding flowfield. For instance, some configurations exhibit a near-monotonic pressure decrease along the surface, typical of gently tapered bodies where the flow undergoes sustained expansion. Others show regions of local recompression or secondary rises in C_p, indicating the presence of geometric deflections—such as flares or slope breaks—that generate weak compression waves or oblique shocks.

In particular, the red geometry displays a pronounced mid-body drop in C_p followed by a rapid decline, characteristic of sharper aft-slopes that induce strong expansion. The green geometry, in contrast, shows a more gradual early decay but a noticeable increase in C_p nearer to the trailing region, suggesting a flare-like feature that reorients the flow and produces localized compression. The blue and orange geometries follow more moderate trends, with smoother transitions and less dramatic

pressure variation, indicative of more continuous shaping.

These examples collectively demonstrate the aerodynamic breadth of the dataset. Small changes in nose curvature, slope angle, or flare magnitude produce distinctly different pressure distributions that would influence integrated loads, heating trends, and shock-structure behavior. The variety of responses shown in Fig. 5 underscores why a sequence-learning model such as a BiLSTM is well-suited for this problem: the network must capture not only the global decay trends but also localized shape-driven features that appear at different positions along the surface.

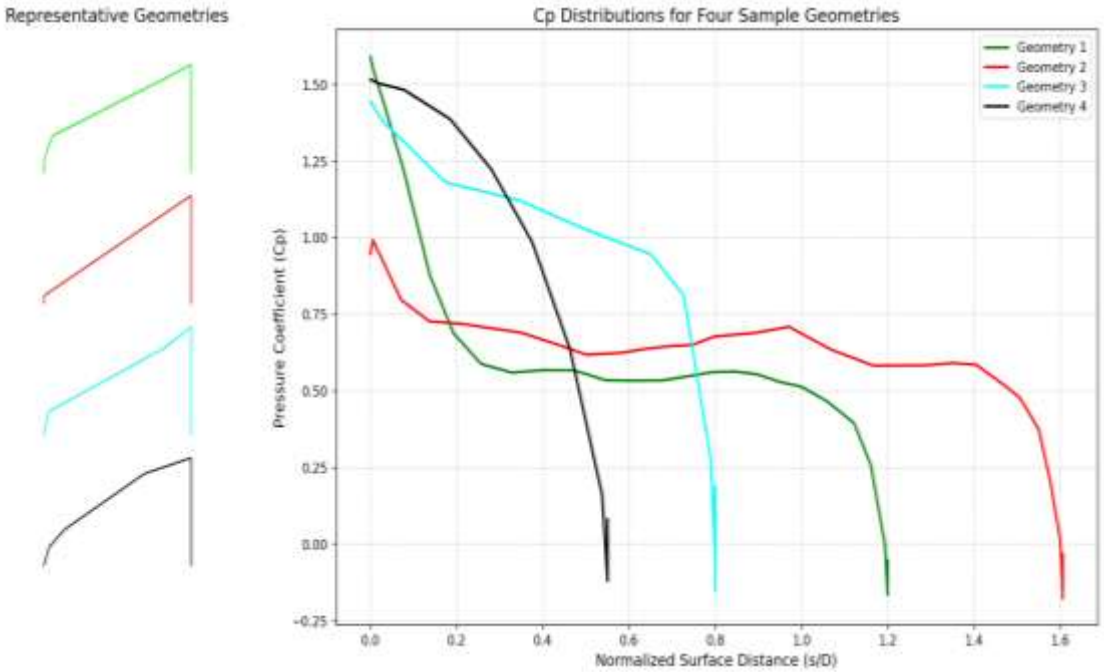


Fig. 6. four representative configurations (left) together with their corresponding surface pressure coefficient (C_p) distributions as a function of normalized surface distance.

4.2 Model prediction

Figure 7 presents the temperature distribution around the shape. A significant rise in temperature is observed near the stagnation point, where the flow decelerates abruptly due to the nature of geometry. This region exhibits maximum thermal loading, with temperatures reaching approximately 377 K. Downstream of the stagnation region, the temperature gradually decreases as the flow expands and moves along the surface. These thermal effects are crucial in understanding the heat transfer behavior and justify the application of Sutherland's law to model temperature-dependent viscosity in the simulation. The temperature contour complements the pressure field analysis and offers valuable insight into the aerodynamic heating mechanisms relevant to high-speed flows.

Figure 8 presents the Mach number contour generated from CFD simulations around. The incoming supersonic flow undergoes a strong deceleration near the stagnation point, where the Mach number drops to nearly zero due to the formation of a detached bow shock. As the flow progresses along the surface, the Mach number increases downstream due to flow expansion and acceleration. The highest Mach numbers are observed away from the body, indicating areas where the flow remains largely undisturbed. This distribution is crucial in identifying regions of compressibility effects, which directly influence the pressure coefficient and heat flux behavior over the body.

The performance of the BiLSTM model was evaluated by comparing the predicted pressure coefficient (C_p) values with those obtained from CFD simulations. Fig. 9a presents the predicted and actual C_p values along the normalized surface

distance (s/D) for a representative geometry. As illustrated, the Bi-LSTM model successfully captures the overall trend of the pressure distribution, with high accuracy across most of the surface. Notably, minor discrepancies appear in the aft body region where C_p becomes negative, which may be attributed to reduced data density or increased flow complexity in that region.

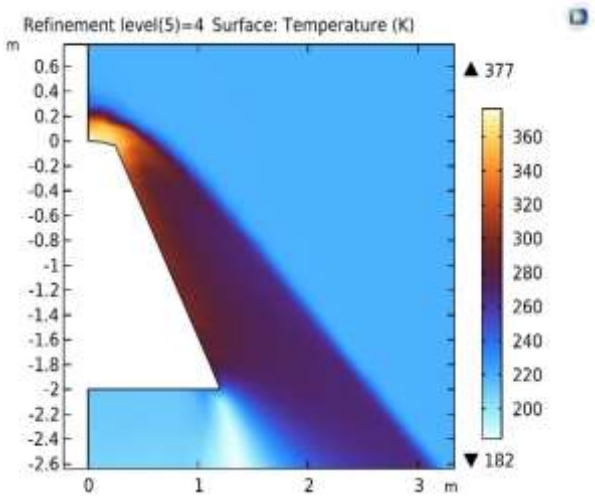


Fig.7. Temperature contour around the body, showing thermal gradients resulting from shock compression and viscous effects. The highest temperatures appear near the stagnation region due to strong flow deceleration and compress.

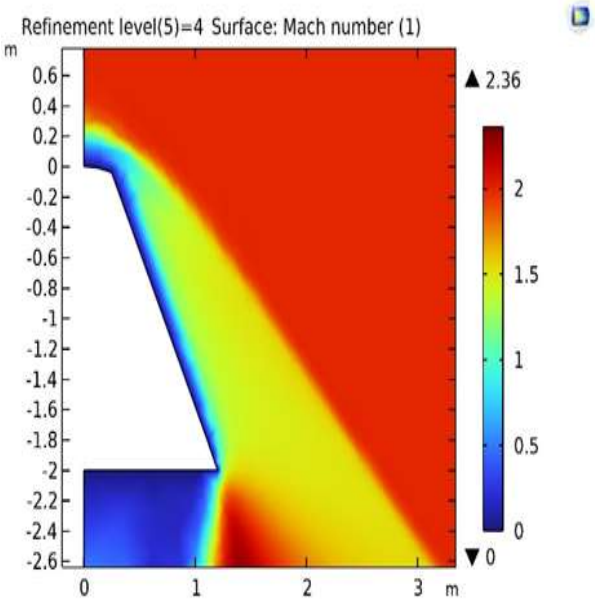
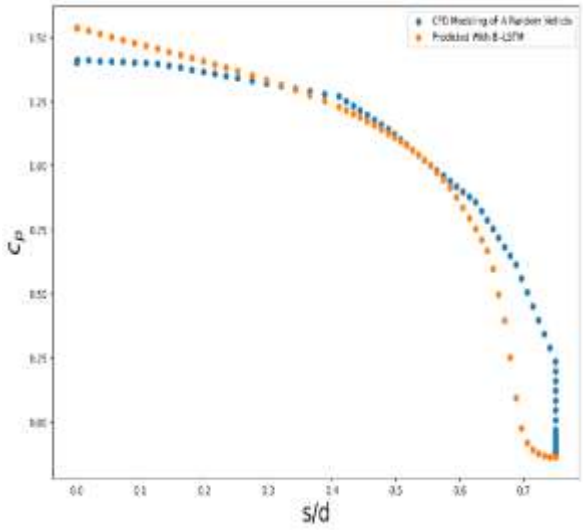


Fig. 8. Mach number distribution around the body, highlighting compressibility effects and shock formation.



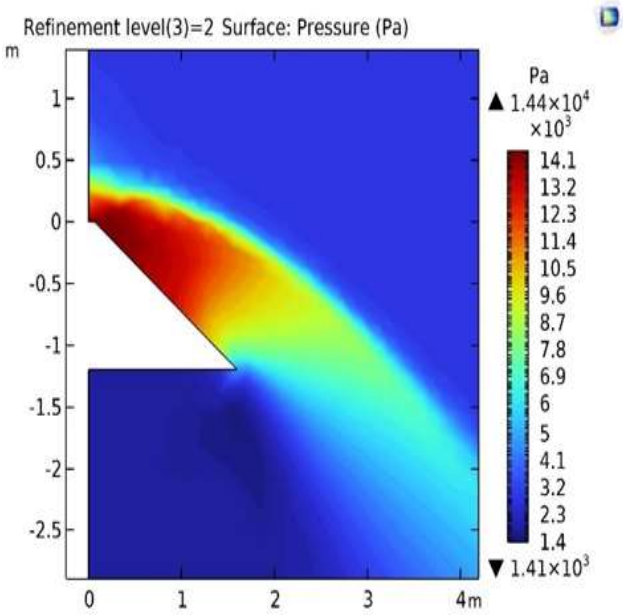


Fig. 9. a) the predicted pressure coefficient (C_p) values with those obtained from CFD simulations for the represented geometry b) Surface pressure distribution (Pa) from CFD simulation for a random geometry (R=1.3m, L=1.2, α=52°, β=52°, D=1.6m, x=0.2m).

To quantify the predictive performance, statistical metrics such as the coefficient of determination (R^2) and the mean absolute error (MAE) were used. The model achieved an R^2 score of 0.985 and an MAE of 0.045, indicating strong agreement between predicted and reference values. The coefficient of determination is defined as:

$$R^2 = 1 - \frac{\sum_{i=1}^{N}(C_{p,i} - \hat{C}_{p,i})^2}{\sum_{i=1}^{N}(C_{p,i} - \bar{C}_{p,i})^2} \quad (13)$$

where $C_{p,i}$ are the true CFD values, $\hat{C}_{p,i}$ are the predicted values, and $\bar{C}_{p,i}$ is the mean of the true values.

Figure 10 shows the training and validation loss curves over the course of 54 epochs. The loss steadily decreased during the initial stages of training and eventually stabilized at a low value for both training and validation sets. This trend indicates that the BiLSTM model successfully learned the underlying patterns in the data without overfitting. The close alignment between the two curves further confirms the generalization capability of the model. The final loss values remained consistent, demonstrating convergence and reliable performance across unseen data.

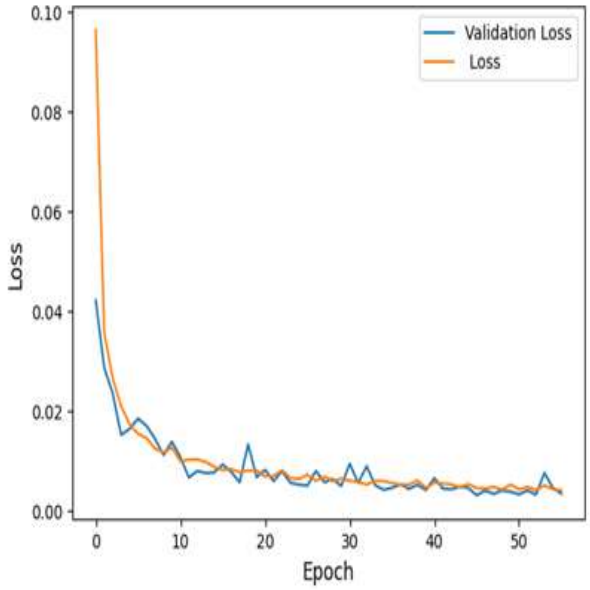


Fig. 10. Training and validation loss curves of the BiLSTM model over 55 epochs.

Figure 11a provides a scatter plot of the predicted versus true C_p values for another geometry, further confirming the model's robustness. Fig. 11b illustrates the pressure distribution over the surface of the blunt body obtained from CFD simulations. As expected, a strong bow shock forms ahead of the body, generating a high-pressure region near the stagnation point, which then gradually decreases along the body's surface. The pressure field captures key flow features such as the shock layer and the expansion downstream, validating the robustness of the numerical solution.

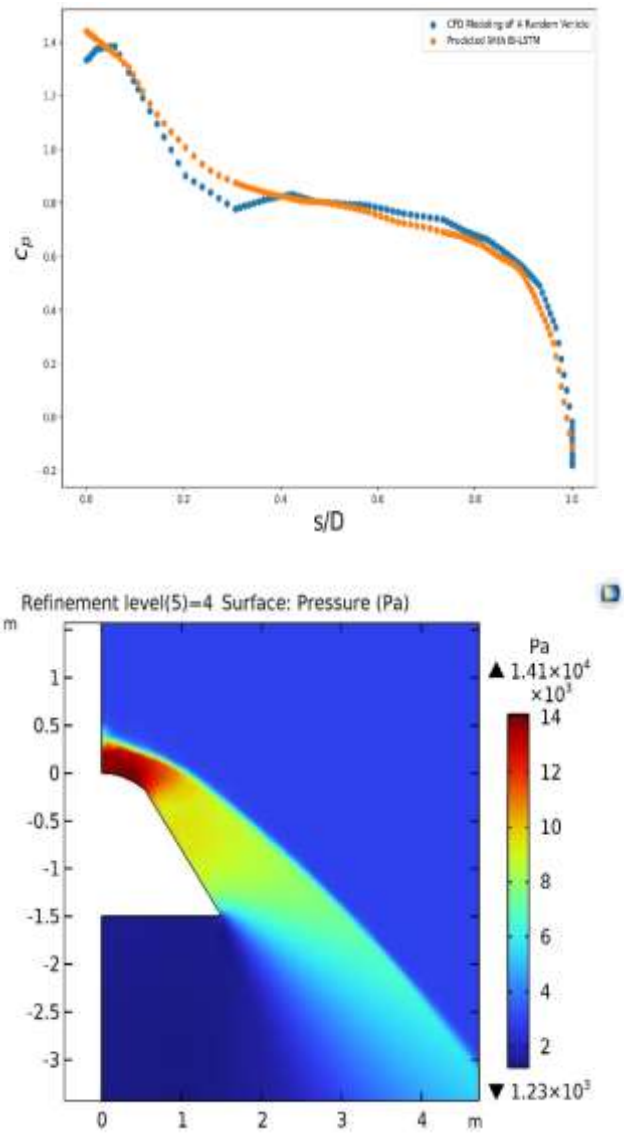


Fig. 11. a) the predicted pressure coefficient (C_p) values with those obtained from CFD simulations for the represented geometry b) Surface pressure distribution (Pa) from CFD simulation for a random geometry (R=0.93m, L=1.5, α=36°, β=35°, D=1.5m, x=0.2m).

4.3 Comparison with Other Neural Architectures

To evaluate the effectiveness of the proposed BiLSTM architecture, comparative experiments were conducted using two baseline models: a conventional feedforward neural network (FNN) and a unidirectional LSTM. All models were trained under identical conditions, using the Adam optimizer (learning rate 0.001), mean-squared error (MSE) loss, and the same dataset split to ensure a fair comparison.

The FNN consisted of three hidden layers with 128, 64, and 32 neurons. The unidirectional LSTM model employed two stacked LSTM layers with 128 and 64 units, followed by the same fully connected layers used in the BiLSTM. Table 1 summarizes the quantitative results.

The BiLSTM achieved the highest overall accuracy, with an R^2 score of 0.985 and a mean absolute error (MAE) of 0.045, outperforming both the LSTM (R^2=0.953, MAE = 0.067) and the FNN (R^2=0.962, MAE = 0.101). Despite having a higher parameter count (307,841 parameters, compared to 122,241 for the LSTM and 15,681 for the FNN), the bidirectional structure enables the model to capture correlations along the normalized surface distance in both forward and backward directions. This capability leads to smoother and more physically consistent C_p predictions, particularly near the stagnation region and across flare-induced compression zones, where flow gradients are strongest.

These results indicate that although simpler architectures can approximate the general trend of the surface pressure distribution, they lack the robustness and spatial awareness provided by the BiLSTM. Additional evaluations on unseen geometries further demonstrated the BiLSTM's superior generalization capability, maintaining high prediction accuracy even for shapes excluded from the training phase.

Table 3. Performance comparison of neural network architectures.

Model	Parameters	R^2	*MAE*
FNN	15681	0.962	0.101
LSTM	122241	0.953	0.067
Bi-LSTM	307841	0.985	0.045

4.4 Multi-Mach Validation of the BiLSTM Surrogate Model

For validation under additional flow conditions, the BiLSTM model was retrained by including new CFD data at Mach 1.5 and Mach 2.5, each containing ten additional geometries not present in the original training set. This expanded dataset improves the model's ability to generalize across a broader range of compressible–flow conditions and enables assessment of Mach-dependent aerodynamic behavior.

Figure 12 compares the BiLSTM-predicted pressure coefficient distributions with high-fidelity CFD results for a representative geometry at Mach 1.5, Mach 2.0, and Mach 2.5. The model successfully captures the overall C_p decay trend along the normalized surface distance s/D, including the stagnation-region peak and the subsequent pressure relaxation toward the aft body. The relative ordering of the curves with respect to Mach number is correctly learned: higher Mach numbers lead to increased compression near the nose and lower pressure recovery downstream, which agrees with established compressible-flow theory.

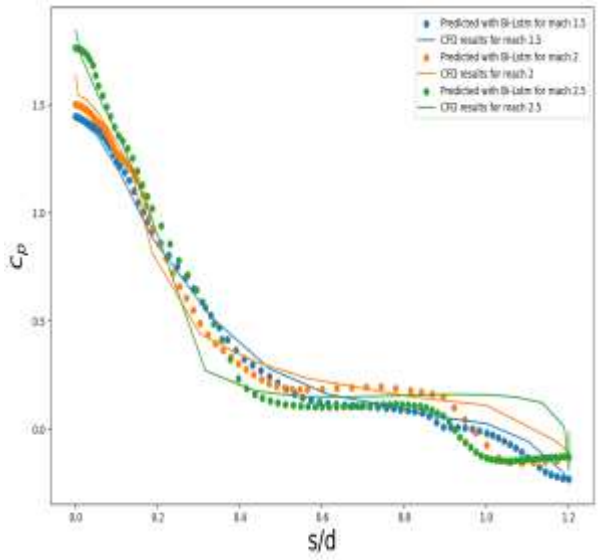


Fig. 12. Comparison of BiLSTM-predicted and CFD-computed pressure coefficient distributions for a representative geometry at Mach 1.5, Mach 2.0, and Mach 2.5 for a random geometry (R=1.3m, L=1.2, α=18°, β=18°, D=1 m, x=0.2m).

However, the pointwise accuracy decreases as the Mach number deviates from the dominant region of the training distribution (initially concentrated around Mach 2). Predictions at Mach 1.5 and Mach 2.5 show small but noticeable differences from the CFD curves, particularly near regions where shock curvature, surface deflection angle, or local expansion effects become more sensitive to Mach number. This behavior is expected because a BiLSTM model trained on limited data cannot fully capture the complex nonlinear dependence of C_p on Mach number, especially in flow regimes involving strong gradients or local shock interactions.

Despite this, the model reproduces the global aerodynamic behavior reliably and demonstrates its capability as a trend-accurate surrogate model across multiple Mach numbers. Increasing the amount of training data at off-design Mach levels, or adopting Mach-conditional architectures such as physics-informed recurrent networks or attention-based encoder–decoder models, would further improve prediction accuracy.

5. CONCLUSION

In this study, a Bidirectional Long Short-Term Memory (BiLSTM) neural network was developed to predict surface pressure coefficient distributions for a wide range of parametrically defined supersonic geometries. A high-fidelity CFD dataset comprising 80 geometries was generated, with solution accuracy ensured through a mesh-independence study. These steps provided a reliable foundation for training the surrogate model.

The BiLSTM architecture was chosen for its ability to capture forward and backward spatial dependencies along the normalized surface coordinate, enabling it to represent the smooth aerodynamic variation more effectively than conventional feedforward networks or unidirectional LSTMs. Comparative evaluations confirmed this advantage: while all models performed reasonably well, the BiLSTM achieved the most accurate and physically consistent predictions, particularly in regions with steep pressure gradients such as the stagnation and flare zones. Overall model performance, with an R^2=0.985 and a mean absolute error of 0.045, demonstrates its strong predictive capability.

The surrogate model closely matched CFD results across the dataset and maintained good accuracy when tested on unseen Mach numbers, highlighting its robustness and generalization potential. By reducing the computational cost associated with repeated CFD evaluations while preserving high fidelity, the proposed BiLSTM framework provides a powerful tool for rapid aerodynamic assessment and early-stage design exploration.

Future work may extend this approach to three-dimensional geometries, incorporate broader flow conditions, or integrate attention-based architectures to further enhance predictive performance and physical interpretability.

CONFLICT OF INTERESTS

No conflict of interest has been expressed by the authors.

REFERENCES

[1] M. M. Rai and N. K. Madavan, “Aerodynamic design using neural networks,” *AIAA Journal*, vol. 38, no. 1, pp. 173-182, 2000, https://doi.org/10.2514/2.938.

[2] L. Hu, J. Zhang, Y. Xiang, and W. Wang, “Neural networks-based aerodynamic data modeling: A comprehensive review,” *IEEE Access*, vol. 8, pp. 90805-90823, 2020, https://doi.org/10.1109/ACCESS.2020.2993562.

[3] S. L. Brunton, B. R. Noack, and P. Koumoutsakos, “Machine learning for fluid mechanics,” *Annual Review of Fluid Mechanics*, vol. 52, no. 1, pp. 477-508, 2020, https://doi.org/10.1146/annurev-fluid-010719-060214.

[4] R. Vinuesa and S. L. Brunton, “Enhancing computational fluid dynamics with machine learning,” *Nature Computational Science*, vol. 2, no. 6, pp. 358-366, 2022, https://doi.org/10.1038/s43588-022-00264-7.

[5] H. Salehi, S. Das, S. Chakrabartty, S. Biswas, and R. Burgueño, “Damage identification in aircraft structures with self-powered sensing technology: A machine learning approach,” *Structural Control and Health Monitoring*, vol. 25, no. 12, 2018, Art. no. e2262, https://doi.org/10.1002/stc.2262.

[6] M. De Jong *et al.*, “A statistical learning framework for materials science: application to elastic moduli of k-nary inorganic polycrystalline compounds,” *Scientific Reports*, vol. 6, no. 1, 2016, Art. no. 34256, https://doi.org/10.1038/srep34256.

[7] J. Kou and W. Zhang, “Data-driven modeling for unsteady aerodynamics and aeroelasticity,” *Aerospace Sciences*, vol. 125, 2021, Art. no. 100725, https://doi.org/10.1016/j.paerosci.2021.100725.

[8] J. Li, X. Du, and J. R. Martins, “Machine learning in aerodynamic shape optimization,” *Aerospace Sciences*, vol. 134, 2022, Art. no. 100849, https://doi.org/10.1016/j.paerosci.2022.100849.

[9] H. Y. Fan, G. S. Dulikravich, and Z. X. Han, “Aerodynamic data modeling using support vector machines,” *Inverse Problems in Science and Engineering*, vol. 13, no. 3, pp. 261-278, 2005, https://doi.org/10.2514/6.2004-280.

[10] Z. Wang, I. Akhtar, J. Borggaard, and T. Iliescu, “Proper orthogonal decomposition closure models for turbulent flows: a numerical comparison,” *Computer Methods in Applied Mechanics and*

Engineering, vol. 237, pp. 10-26, 2012, https://doi.org/10.1016/j.cma.2012.04.015.

[11] E. Andrés-Pérez and C. Paulete-Periáñez, "On the application of surrogate regression models for aerodynamic coefficient prediction," *Complex & Intelligent Systems*, vol. 7, no. 4, pp. 1991-2021, 2021, https://doi.org/10.1007/s40747-021-00307-y.

[12] A. Teimourian, D. Rohacs, K. Dimililer, H. Teimourian, M. Yildiz, and U. Kale, "Airfoil aerodynamic performance prediction using machine learning and surrogate modeling," *Heliyon*, vol. 10, no. 8, 2024, https://doi.org/10.1016/j.heliyon.2024.e29377.

[13] J. Zhang and X. Zhao, "Machine-learning-based surrogate modeling of aerodynamic flow around distributed structures," *AIAA Journal*, vol. 59, no. 3, pp. 868-879, 2021, https://doi.org/10.2514/1.J059877.

[14] M. F. Negoita and M. V. Hothazie, "A machine learning-based approach for predicting aerodynamic coefficients using deep neural networks and cfd data," *INCAS Bulletin*, vol. 16, no. 4, 2024, https://doi.org/10.13111/2066-8201.2024.16.4.9.

[15] D. Pereira, F. Afonso, and F. Lau, "End-to-end deep-learning-based surrogate modeling for supersonic airfoil shape optimization," *Aerospace*, vol. 12, no. 5, 2025, Art. no. 389, https://doi.org/10.3390/aerospace12050389.

[16] D. A. Sterpu, D. Măriuța, G. Cican, C. M. Larco, and L.-T. Grigorie, "Machine learning prediction of airfoil aerodynamic performance using neural network ensembles," *Applied Sciences*, vol. 15, no. 14, 2025, Art. no. 7720.

[17] G. Catalani, J. Fesquet, X. Bertrand, F. Tost, M. Bauerheim, and J. Morlier, "Towards scalable surrogate models based on Neural Fields for large scale aerodynamic simulations," *Computers & Fluids*, 2025, Art. no. 106929, https://doi.org/10.1016/j.compfluid.2025.106929.

[18] P. Bo, Y. Zhang, L. Junlin, W. Xudong, M. Chang, and B. Junqiang, "Data-driven surrogate model for aerodynamic design using separable shape tensor method," *Chinese Journal of Aeronautics*, vol. 37, no. 9, pp. 41-58, 2024, https://doi.org/10.1016/j.cja.2024.03.014.

[19] X. Hui, J. Bai, H. Wang, and Y. Zhang, "Fast pressure distribution prediction of airfoils using deep learning," *Aerospace Science and Technology*, vol. 105, 2020, Art. no. 105949, https://doi.org/10.1016/j.ast.2020.105949.

[20] K. Li, J. Kou, and W. Zhang, "Deep neural network for unsteady aerodynamic and aeroelastic modeling across multiple Mach numbers," *Nonlinear Dynamics*, vol. 96, pp. 2157-2177, 2019, https://doi.org/10.1007/s11071-019-04915-9.

[21] A. T. Mohan and D. V. Gaitonde, "A deep learning based approach to reduced order modeling for turbulent flow control using LSTM neural networks," *Arxiv Preprint Arxiv:1804.09269*, 2018, https://doi.org/10.48550/arXiv.1804.09269.

[22] Z. Deng, Y. Chen, Y. Liu, and K. C. Kim, "Time-resolved turbulent velocity field reconstruction using a long short-term memory (LSTM)-based artificial intelligence framework," *Physics of Fluids*, vol. 31, no. 7, 2019, https://doi.org/10.1063/1.5111558.

[23] S. Pawar, S. M. Rahman, H. Vaddireddy, O. San, A. Rasheed, and P. Vedula, "A deep learning enabler for nonintrusive reduced order modeling of fluid flows," *Physics of Fluids*, vol. 31, no. 8, 2019, https://doi.org/10.1063/1.5113494.

[24] J. Wang, C. He, R. Li, H. Chen, C. Zhai, and M. Zhang, "Flow field prediction of supercritical airfoils via variational autoencoder based deep learning framework," *Physics of Fluids*, vol. 33, no. 8, 2021, https://doi.org/10.1063/5.0053979.

[25] K. Taunk, S. De, S. Verma, and A. Swetapadma, "A brief review of nearest neighbor algorithm for learning and classification," in *International Conference on Intelligent Computing and Control Systems (ICCS)*, Madurai, India, 2019, Paper 1255-1260, 10.1109/ICCS45141.2019.9065747.

[26] J. A. Sánchez Muñoz, C. Lagarza-Cortés, and J. Ramírez-Cruz, "Aerodynamic drag coefficient prediction of a spike blunt body based on k-nearest neighbors," *Aerospace*, vol. 11, no. 9, 2024, Art. no. 757, 10.3390/aerospace11090757.

[27] A. Kashefi, D. Rempe, and L. J. Guibas, "A point-cloud deep learning framework for prediction of fluid flow fields on irregular geometries," *Physics of Fluids*, vol. 33, no. 2, 2021, https://doi.org/10.1063/5.0033376.

[28] Y. Shen, W. Huang, Z.-g. Wang, D. f. Xu, and C. Y. Liu, "A deep learning framework for aerodynamic pressure prediction on general three-dimensional configurations," *Physics of Fluids*, vol. 35, no. 10, 2023, https://doi.org/10.1063/5.0172437.

[29] R. Mehta, "Numerical simulation of supersonic flow past reentry capsules," *Shock Waves*, vol. 15, no. 1, pp. 31-41, 2006.

[30] H. Shi, M. Xu, and R. Li, "Deep learning for household load forecasting—A novel pooling deep RNN," *IEEE Transactions on Smart Grid*, vol. 9, no. 5, pp. 5271-5280, 2017, https://doi.org/10.1109/TSG.2017.2686012.

[31] J. S. Zhang and X. C. Xiao, "Predicting chaotic time

series using recurrent neural network," *Chinese Physics Letters*, vol. 17, no. 2, 2000, Art. no. 88, https://doi.org/10.1109/NNSP.1992.253669.

[32] A. Graves, *Supervised Sequence Labelling*. Springer, 2012.

[33] S. Hochreiter, Y. Bengio, P. Frasconi, and J. Schmidhuber, "Gradient flow in recurrent nets: The difficulty of learning long-term dependencies," in *A Field Guide to Dynamical Recurrent Neural Networks*. IEEE Press In, 2001, https://doi.org/10.1109/9780470544037.ch14.

[34] S. Hochreiter and J. Schmidhuber, "Long short-term memory," *Neural Computation*, vol. 9, no. 8, pp. 1735-1780, 1997, https://doi.org/10.1162/neco.1997.9.8.1735.